Journal of Materials Science: Materials in Electronics (2019) 30:13056–13066
https://doi.org/10.1007/s10854-019-01667-5

One-step phosphorylation of graphene oxide for the fabrication of nanocomposite membranes with enhanced proton conductivity for fuel cell applications

Saad Ahmed[1] · Yangben Cai[1] · Muhammad Ali[1] · Santosh Khannal[1] · Zaheer Ahmad[2] · Yunhua Lu[1] · Songnan Wang[1] · Shiai Xu[1,3]

Received: 30 January 2019 / Accepted: 5 June 2019 / Published online: 22 June 2019

Abstract
In this work, graphene oxide (GO) was phosphorylated by a novel method and then incorporated into the chitosan (CS) matrix for the fabrication of nanocomposite membranes with enhanced proton conductivity for fuel cell applications. The 2D phosphorylated graphene oxide (PGO) offers efficient proton hopping sites ($–PO_3H^{-}\cdots{}^{+}H_3N$-) that form continuous proton conducting channels at the CS/PGO interface. The CS/PGO nanocomposite membrane containing 2 wt% of PGO shows an optimum proton conductivity of 0.036 S cm^{-1}, which is higher than that of commercial Nafion 117 membrane (0.033 S cm^{-1}). In comparison with CS control membrane, CS/PGO nanocomposite membranes have higher thermal and mechanical stability because of the strong electrostatic and hydrogen bonding interactions between $–NH_2$ of CS and $–PO_3H_2$ of GO. This study provides a new facile way to fabricate high-performance, low-cost and eco-friendly nanocomposite membranes for fuel cell applications.

1 Introduction

Conductive materials play an important role in various chemical and biological processes and energy based devices [1, 2]; and importantly, they can also be used as the next generation materials in proton exchange membrane fuel cells (PEMFC) [3–8]. The polymer electrolyte membrane (PEM) is a key component of PEMFC responsible for proton conduction and separation of oxidizing agents and fuels [9–11]. Thus, it is desirable for PEM to have high proton conductivity and thermal stability. At present, Nafion membranes are the most commonly used due to their outstanding performance, high proton conductivity, and extraordinary thermal and chemical stability [12, 13]. However, their applications in PEMFC are limited by their high cost and low proton conductivity at high temperatures (> 100 °C) [14, 15]. Thus, there is a need to develop PEMs with high proton conductivity and appropriate thermal and mechanical stability [16, 17].

The phosphoric acid group is considered a better proton conductor than many other acidic groups due to its excellent self-ionization, proton solvation capability and intermolecular hydrogen bonding [1, 18, 19]. It has a lower energy penalty (37.2 kJ mol^{-1}) than the sulfonic acid group (69.9 kJ mol^{-1}) [20–22], which allows for easier transfer of protons from "acid to acid" [22]. It also has a higher water binding energy (47.3 kJ mol^{-1}) than the sulfonic acid group (44.4 kJ mol^{-1}), indicating an improved water retention ability [20, 23]. Phosphonic acid group can be introduced by (1) incorporating liquid phosphoric acid into polymer membrane, (2) binding phosphoric acid group to various polymer backbone, and (3) grafting phosphonic acid group into inorganic nanofillers [24–32]. Grafting phosphoric acid group onto nanofillers is effective in enhancing proton conductivity and mechanical stability of membranes [33].

It is important to develop facile proton transport pathways in order to achieve desirable proton conductivity. However, some low-cost materials such as chitosan (CS), sodium alginate and poly vinyl alcohol (PVA) may have

✉ Shiai Xu
saxu@ecust.edu.cn

[1] Shanghai Key Laboratory of Advanced Polymeric Material, School of Materials Science and Engineering, East China University of Science and Technology, Shanghai 200237, China

[2] Department of Chemistry, University of Wah, Wah Cantt 47040, Pakistan

[3] School of Chemical Engineering, Qinghai University, Xining 810016, China

low proton conductivity due to lack of continuous transport channels. Very often, the conductivity of these materials can be improved by incorporating acid-functionalized nanofillers (mostly sulfonic and phosphonic acid) into the polymer matrix [34, 35] to enhance the transfer efficiency and structural stability of the resultant membranes by interfering with chain mobility and order packing [36–38].

In recent years, graphene oxide (GO) with a 2D sheet structure, high proton conductivity and electronic insulation has been widely used a nanofiller in PEM, and epoxy, hydroxyl and carboxylic acid groups have also been used for structural modification [39–42]. It is shown that the incorporation of sulfonated or phosphonated graphene oxides (SGO, PGO) into CS based membranes can enhance the proton conductivity [43, 44]. CS can act as the membrane matrix owing to its good film-making ability, cost effectiveness and eco-friendliness. It also has good thermal and mechanical strength, as well as acceptable mechanical strength. However, the absence of mobile protons in its structure may lower its proton conductivity and thus restrict its direct use in PEMFC [37, 45, 46].

In the present study, a novel approach was proposed for the preparation of PGO. Phosphonic acid groups was grafted onto GO surface in a single step using ATMP [aminotris(methylenephosphonic acid)]. A facile solution casting method was used for fabrication of a series of CS/PGO nanocomposite membranes by incorporating PGO into CS matrix followed by cross-linking with sulfuric acid. The effect of PGO content on the microstructures and physicochemical characteristics of these CS/PGO nanocomposite membranes were examined. The PGO and CS/PGO nanocomposite membranes were characterized by Fourier transform infrared (FTIR) spectroscopy, energy-dispersive X-ray (EDX) spectroscopy, X-ray diffraction (XRD) analysis, scanning electron microscopy (SEM), and thermogravimetric analysis (TGA). The interfacial interaction between $–PO_3H_2$ group of PGO and $–NH_2$ group of CS could offer new proton conducting pathways. Therefore, the proton conductivity and thermal strength can be improved by incorporating PGO into the CS matrix. (Table 1).

Table 1 Thermal properties of GO and PGO

Serial no.	$T_{5\%}$	Char residue (wt%)			
		500 °C	600 °C	700 °C	800 °C
GO	87.20	59.41	58.09	56.76	56.39
PGO	126.46	77.59	63.48	41.01	23.31

2 Experimental

2.1 Materials and chemicals

CS with a deacetylation of ≥ 80% was supplied by Aladdin Chemical Reagent Co., (China). Acetic acid (99%) and sulfuric acid (98%) were purchased from Macklin Biochemical Co., Ltd., (China). ATMP solution (50 wt% of ATMP in H_2O) was supplied by Dramas Beta Chemical Reagent Co., Ltd., (China). GO flakes were supplied by XF NANO Science and Technology Ltd., (China). Deionized water was used throughout the experiments.

2.2 Synthesis of PGO

GO was phosphorylated as follows. GO sheets (1.0 g) were immersed in ATMP acid solution (25 wt% of ATMP in H_2O) under sonication at 300 W and 40 Hz for 12 h at room temperature, and then centrifuged and rinsed with deionized water several times until it became neutral. Finally, the obtained PGO was vacuum dried for 24 h at 80 °C. The reaction scheme is shown in Fig. 1.

2.3 Preparation of CS/PGO membranes

The membranes were fabricated as described previously [47]. Typically, 1.25 g of CS was dissolved in 50 mL of water containing 2 mL of acetic acid solution for 24 h at room temperature. Instantaneously, a certain amount of PGO was dispersed ultrasonically in 50 mL of deionized water. After that, the two solutions were mixed and stirred for 48 h at room temperature. The resultant solution was cast on a clear glass plate and dried at 30 °C for 72 h. The obtained membranes were crosslinked with 1.0 M sulfuric acid solution for 24 h at room temperature (Fig. 2.), washed with deionized water to remove residual sulfuric acid, and then oven dried at 30 °C for 24 h. The obtained nanocomposite

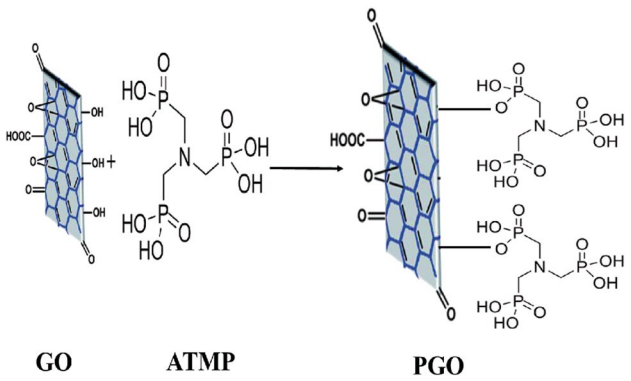

Fig. 1 Schematic for the phosphorylation of GO

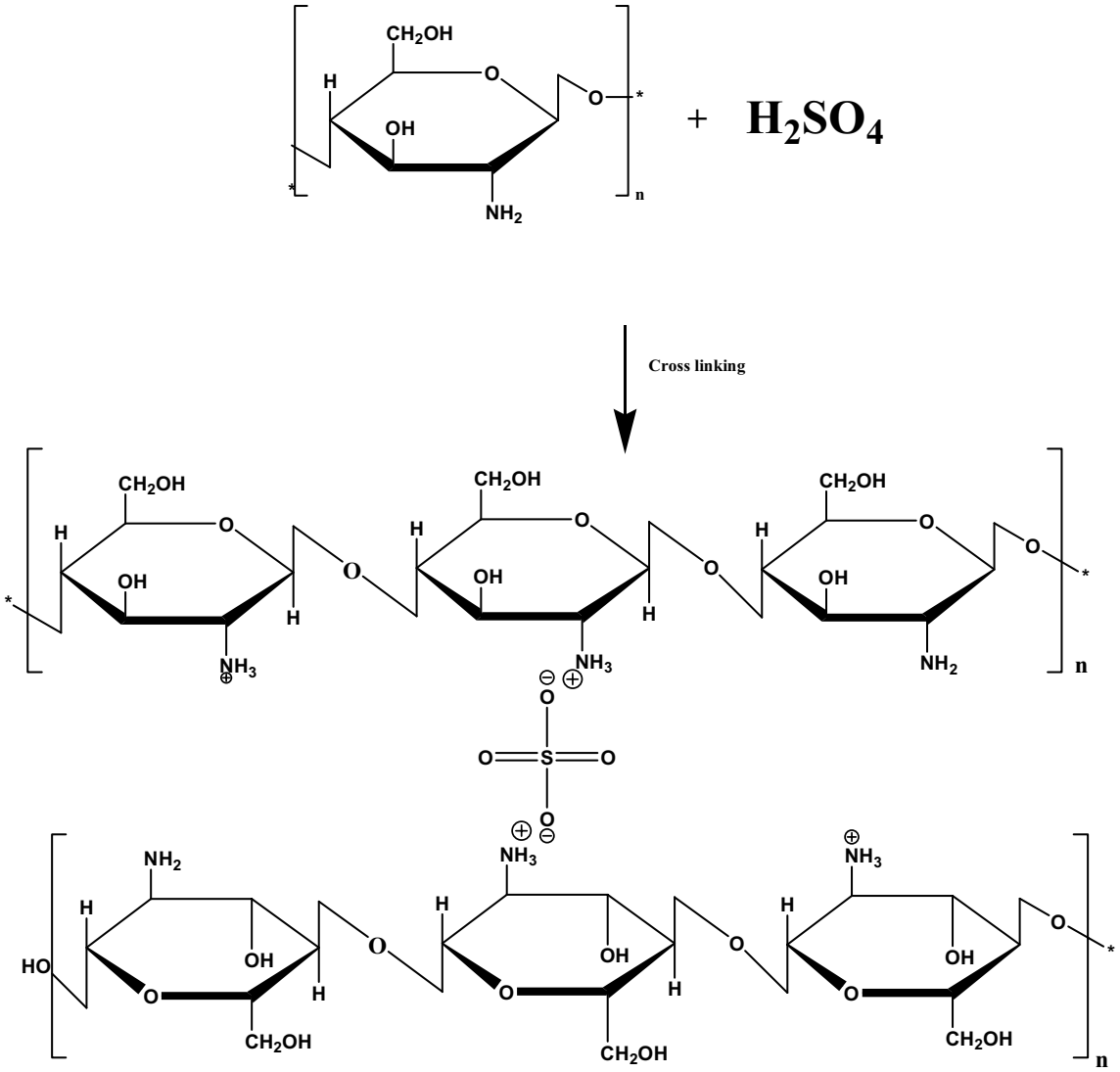

Fig. 2 Cross-linking reaction between CS and H_2SO_4

membranes were named as CS/PGO-X, where X (1.0, 1.5, 2.0 and 2.5) denoted the weight ratio of PGO to CS. For comparison, CS control membrane was also prepared by the same method but without the incorporation of nano sheets.

2.4 Characterization and measurements

The FTIR spectra of ATMP, PGO and CS/PGO nanocomposite membranes were recorded at a scan rate of 4 cm^{-1} in the range of 500–4000 cm^{-1} at room temperature using a Nicolet 6700 FTIR spectrometer in transmittance mode. The crystalline structures of CS/PGO nanocomposite membranes were determined on a Rigaku D/max advanced wide-angle X-ray diffractometer (XRD) using a nickel-filtered Cu K radiation (40 kV, 200 mA). TGA was conducted with a TA 50 thermogravimetric analyzer under a nitrogen atmosphere at a rate of 10 °C min^{-1} from 25 to 800 °C. The surface properties of GO and PGO were determined by X-ray photoelectron spectroscopy (XPS) using an ESCALAB 250Xi instrument with an Al Kα radiation source followed by 0.05 eV as an energy step size for high resolution XPS. The valence bond spectrum (VBS) was received from the lower binding energy portion (−10 to 33 eV) of the full XPS spectrum. The morphology of PGO was characterized by TEM using a JEM-2100 transmission electron microscope at an accelerating voltage of 200 kV. PGO was dispersed in water, and the dispersion was dropped onto a 200-mesh copper grid with a carbon supporting film, and excess liquid was removed by filter paper and dried under an infrared lamp. The cross-sectional morphologies of CS/PGO nanocomposite membranes were observed under a scanning electron microscope (FE-S4800, Hitachi). Prior to analysis, all samples were fractured

in liquid nitrogen and vacuum-sputtered with a layer of gold. The mechanical properties of CS/PGO nanocomposite membranes were measured with a MTS E43 universal testing machine according to Chinese standard GB.T.1040.3 at an initial speed of 2 mm/min at room temperature. The average and standard deviation of five measurements were reported.

The water uptake of CS/PGO nanocomposite membranes was calculated by the weight difference between membranes dried under vacuum and those immersed in de-ionized water for 48 h at room temperature. Note that the surface water of the membrane was quickly removed with a tissue paper for the measurement of weight. The area swelling was determined by the same procedure except that the area was considered instead of weight. The water uptake and swelling ratio were determined from Eqs. 1 and 2, respectively.

$$\text{Water uptake}\ (\%) = \frac{W_{\text{wet}} - W_{\text{dry}}}{W_{\text{dry}}} \times 100 \tag{1}$$

$$\text{Area swelling}\ (\%) = \frac{A_{\text{wet}} - A_{\text{dry}}}{A_{\text{dry}}} \times 100 \tag{2}$$

where W_{wet} and A_{wet} are the weight and area of the membranes soaked in de-ionized water for 48 h, and W_{dry} and A_{dry} are the weight and area of the dried membranes, respectively.

The ion exchange capacity (IEC) of CS/PGO nanocomposite membranes was determined via the typical acid–base titration method. The nanocomposite membranes were immersed in 2.0 M NaCl solution for 48 h to exchange H^+ in the membrane for Na^+, and then the solution was titrated with 0.01 M NaOH using phenolphthalein as an indicator. The IEC (mmol g^{-1}) was calculated from Eq. 3.

$$\text{IEC}\left(\text{mmol g}^{-1}\right) = \frac{0.01 \times 1000 \times V_{\text{NaOH}}}{W_{\text{dry}}} \tag{3}$$

where V_{NaOH} is the volume of NaOH solution used, and W_{dry} is the weight of dry membrane, respectively.

The in plane proton conductivity of CS/PGO nanocomposite membranes was measured by electrochemical impedance spectroscopy using a PARSTAT 2273 electrochemical analyzer (AMETEK, Inc., America) at an oscillating voltage of 20 mV and a frequency range of 10 Hz–1 MHz at room temperature. Prior to measurement, all membranes (2 cm × 0.5 cm) were equilibrated in water for 48 h at room temperature. The resistance was measured from higher frequency intercept of the impedance with the real axis. The in-plane proton conductivity (σ, S cm^{-1}) was determined by the following formula,

$$\sigma = \frac{L}{RA} \tag{4}$$

where R is the measured resistance, L and A are the thickness and area of the membrane, respectively.

3 Results and discussion

3.1 Structural characterization of PGO

The grafting of phosphonic acid group on the GO surface was confirmed by FTIR, XRD, TGA, XPS, TEM and EDX analysis. The FTIR spectra of GO show abundant epoxy, carboxyl and hydroxyl groups, which is in accordance with previous results [48]. The characteristic peak at 1713 cm^{-1} can be attributed to the C=O vibration; while those at 1465 and 3414 cm^{-1} can be attributed to the OH bending and stretching vibration, respectively [49]. After modification with ATMP, the characteristic peaks of phosphonic acid are observed at 941, 997 and 1168 cm^{-1}, indicating the successful grafting of phosphonic acid group with a substantial decrease in hydroxyl group on the GO surface (Fig. 3) [50].

The crystalline pattern of GO and PGO was characterized by XRD. GO shows similar graphitic peaks according to JCPDS Card No. 75-1621, as shown in Fig. 4. The characteristic peak is observed at about $2\theta = 5.42°$ with a basal spacing of 1.63 nm, which is larger than that of graphite (0.423 nm, $2\theta = 21.32°$) [51]. The interlayer distance of GO is remarkably increased during chemical oxidation. The regular stacks of GO may be destroyed during exfoliation, resulting in a decrease or even disappearance of the diffraction peak. The introduction of the monomer to the GO nano sheets leads to the destruction of regular stacks [52], and hence the characteristic peak at $2\theta = 5.42°$ may disappear completely [34]. Other diffraction peaks at $2\theta = 21.32°$ and $2\theta = 43.13°$ are associated with the hexagonal graphite structure and diffraction, respectively. After modification with ATMP, the characteristic peak at 21.32° shifts to 22.31°,

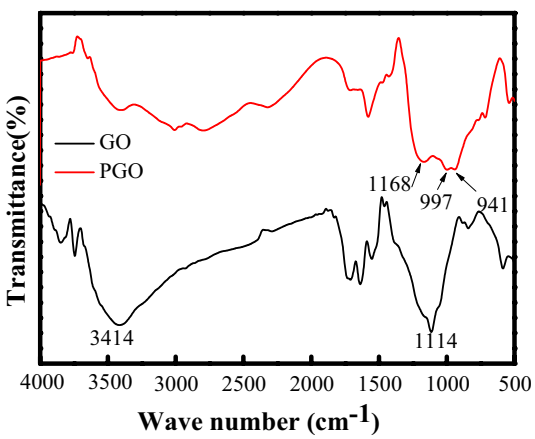

Fig. 3 FTIR of GO, ATMP and PGO

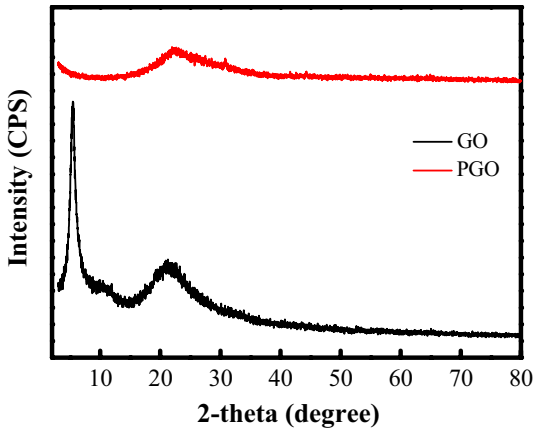

Fig. 4 XRD of GO and PGO

and accordingly the interlayer distance in PGO is slightly decreased from 0.423 to 0.405 nm. This can be attributed to the gradual removal of –OH functional groups [53], resulting in a slight decrease of the inter-layer distance of PGO.

The grafting of ATMP on the GO surface was also confirmed by XPS analysis (Fig. 5). GO exhibits only C 1*s* and O 1*s* bands at 284 and 532 eV, respectively, which is in agreement with earlier literature [54, 55]. After phosphorylation, PGO also shows the P 2*p* and P 2*s* bands at 133 eV and 192 eV due to P–C and P–O bonding; while the N-1*s* band at 401 eV due to N–C bonding [34, 56, 57]. The weight percentage of P is about 18.5%, suggesting that the $–PO_3H_2$ amount grafted on PGO is about 48.1%. These results suggest that ATMP is successfully grafted on GO surface.

The thermal stability of ATMP and PGO was determined by TGA (Fig. 6) and Table 1, respectively. After phosphorylation, PGO undergoes three degradation stages. The first stage is attributed to the loss of moisture at 30–150 °C, resulting in a higher weight loss (93.94%) compared with that of GO (88.46%) due to the higher water adsorption capacity of phosphonic acid group [58]. The second step is attributed to the deoxygenation of GO at 180–280 °C [47]. However, the PGO layer can retard the degradation of oxygenated functional group, and PGO also has a higher weight loss (87.56%) than GO (63.84%). At temperatures higher than 300 °C, the weakening of the inter-sheet interactions can disturb the stacking of GO sheets, resulting in decomposition of nano sheet backbone. By comparison, the char yield of PGO (23.31%) is much lower than that of GO (56.39%), indicating the presence of abundant phosphonic acid groups on GO surface.

The morphologies of GO and PGO were observed by TEM. Figure 7a, c shows that GO is exfoliated into nano sheet with some obvious wrinkles, and the morphology of PGO is similar to that of GO, indicating that no changes occurs in the nano sheet structure during phosphorylation. Since phosphorylation mainly occurs on the GO surface, the structure of nanosheet has slightly changed during modification. After modification, the color of PGO becomes slightly darker (Fig. 7b, d).

The EDX results of GO and PGO are shown in Table 2. It can be seen that GO contains no nitrogen and phosphorus, while PGO contains nitrogen and phosphorus resulting from the reaction with ATMP.

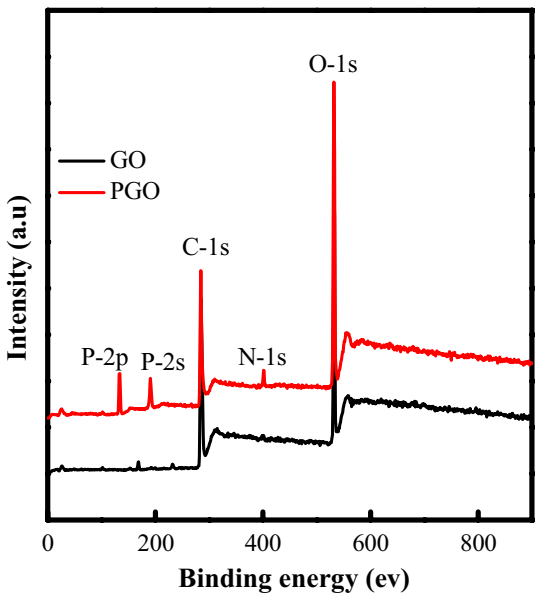

Fig. 5 XPS of GO and PGO

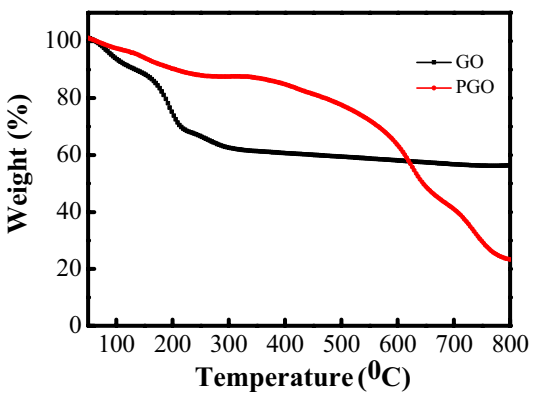

Fig. 6 TGA spectra of GO, ATMP and PGO

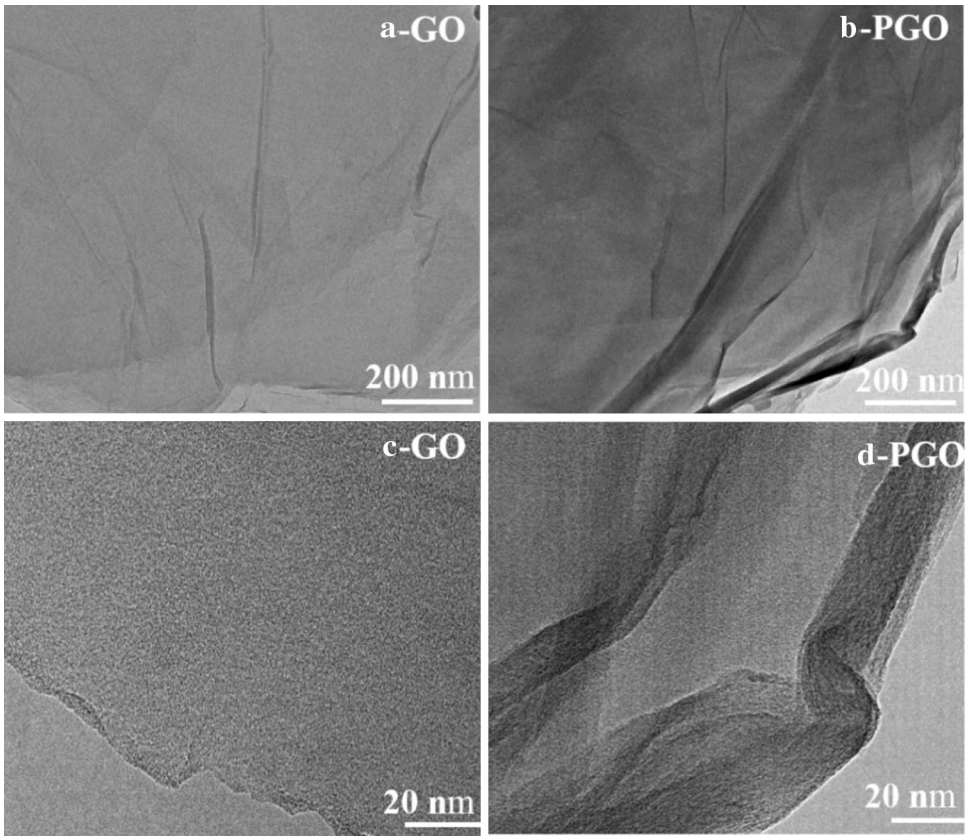

Fig. 7 TEM photographs (**a**, **b**) of GO and PGO at higher resolution (**c**, **d**) at lower resolution

Table 2 The weight composition (%) of different elements in GO and PGO

Serial no.	C	O	N	P
GO	45.05	54.95	–	–
PGO	30.45	46.19	4.43	18.63

3.2 Characterization of CS/PGO nanocomposite membranes

3.2.1 Structure and morphology of CS/PGO nanocomposite membranes

Figure 8 shows the FTIR spectra of a series of CS based membranes with various nano sheet contents. The characteristic peaks at 1040, 1582 and 1670 cm^{-1} can be attributed to the C–O stretching, amide II and amide I [59]. While those bands at 2877 and 2921 cm^{-1} are due to the symmetric and asymmetric stretching of C–H, respectively. After crosslinking with sulfuric acid, the typical symmetric and asymmetric vibrations of NH_3^+ are also observed at 1520 and 1644 cm^{-1} in CS and nanocomposite membranes, respectively, which are attributed to change in hydrogen bond structure and intensity in CS molecules [60]. Increasing the PGO content can enhance the interfacial

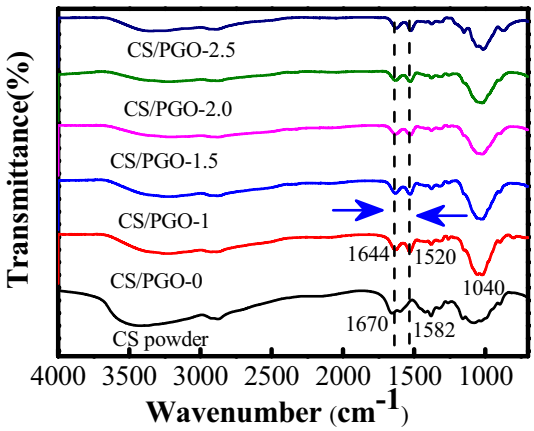

Fig. 8 The FTIR spectra of CS/PGO nanocomposite membranes

interaction, ultimately resulting in a shift of the bands at 3600–3000 cm^{-1} and 1670–1582 cm^{-1} to lower wavenumbers in CS/PGO nanocomposite membranes. This phenomena is mainly due to: (1) electrostatic interactions among the positively charged ammonium groups of CS backbone and the negatively charged phosphonic acid groups; and (2) hydrogen bonding interaction among the $–PO_3H_2$ groups on GO surface and the –OH or $–NH_2$ groups of CS [34]. However no new peak appears, suggesting that CS/PGO

nanocomposite membranes are mixed physically without the formation of any covalent bonds and thus they interact with each other by acid–base pairs.

The proton conductivity of the membrane strongly depends on the diffusion of water molecules and proton mobility that mostly occurs in the amorphous phase rather than in the crystalline phase. The high crystallinity of untreated CS is associated with the strong intramolecular and intermolecular interactions. In order to minimize the crystalline ability of CS, the cross linker sulfuric acid and PGO were used [61, 62], and the crystalline structure and chain packing of CS/PGO nanocomposite membranes were tested by XRD analysis. Figure 9 shows that the characteristic peaks are present at 11.7°, 18.6° and 22.7° in all nanocomposite membranes, which is in good agreement with previous results [63]. The band at 11.7° represents the hydrated crystalline region, while that at 22.7° represents the amorphous structure of CS. Increasing the PGO content causes a reduction in the intensity of these characteristic peaks due to the interference of PGO with CS chain packing, resulting in the disruption of the ordered stacking of the CS chain and ultimately a reduction in the crystalline region.

The distribution of nano sheets and interfacial bonding of the CS/PGO nanocomposite membranes were determined by SEM. Figure 10a–e show the SEM images of cryo-fractured surfaces of CS and CS/PGO nanocomposite membranes with a PGO content of 1.0, 1.5, 2.0, and 2.5 wt%, respectively. The pure CS membrane displays a homogeneous and void free surface; while the addition of PGO leads to the formation of some obvious wrinkles and thus a rough surface for the nanocomposite membranes. Overall, the CS/PGO nanocomposite membranes display a uniform morphology without any cracks. Most PGOs are tightly bound to the CS matrix, suggesting the strong interfacial interaction between PGO and CS. The homogeneous dispersion of PGO offers more continuous pathways for proton transfer.

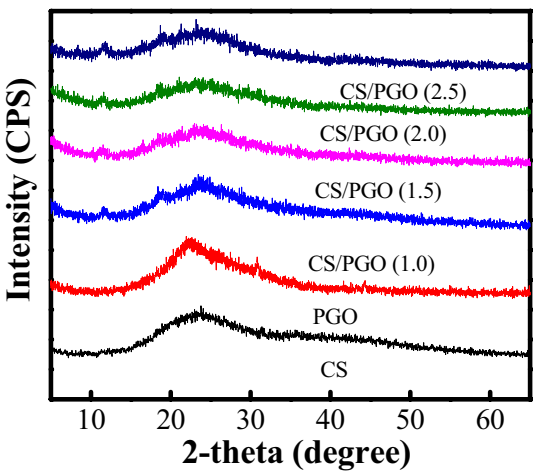

Fig. 9 XRD of CS/PGO nanocomposite membranes

3.2.2 Thermal and mechanical stability of CS/PGO nanocomposite membranes

Obviously, it is necessary for PEMs to be able to withstand high temperatures. The TGA curves of CS/PGO nanocomposite membranes with different PGO contents are shown in Fig. 11. All nanocomposite membranes undergo a three-stage degradation process, as reported in previous studies [64]. The first stage occurs at 30–150 °C due to the evaporation of adsorbed water in the nanocomposite membranes; the second stage occurring at 200–330 °C is attributed to the degradation of CS side chains; while the last stage occurring at 330–800 °C is due to the degradation of polymer backbones. CS usually contains two types of water (free and bound water). The free water can be easily removed at low temperature, whereas the bound water is removed only at high temperature. TGA was performed under a flowing nitrogen atmosphere, and thus the free water can volatilize at low temperature (e.g., 30 °C) although its boiling point is 100 °C. Due to the presence of free and bound water, the nanocomposite membranes show the loss of water in a wide temperature range. Similar phenomena were also reported in our previous study [35]. However, the nanocomposite membranes show higher thermal stability compared to CS control membrane due to (1) homogeneous dispersion of PGO; and (2) strong electrostatic interaction between PGO and CS that can inhibit the degradation of nanocomposite membranes and thus result in a higher char yield of nanocomposite membranes than that of CS membrane. For instance, the char yield of CS at 800 °C is 26.43%, while increasing the PGO content from 1.0 to 2.5 wt%, results in an increase in the char yield from 28.91 to 31.26%.

The tensile strength and elongation at break of the CS/PGO nanocomposite membranes are shown in Table 3. The cross linked CS membrane has a tensile strength of 32.70 MPa and an elongation at break of 8.19%, respectively. Increasing the PGO content can increase the tensile strength up to 61 MPa (2.5 wt%) due to the toughening and reinforcing effect of PGO homogenously dispersed in the CS matrix. The phosphonic acid group can form hydrogen and electrostatic interactions with active groups such as $–NH_2$ and –OH of the CS chain. The crosslinking and the strong interaction between active groups of the CS chain and PGO can hinder the chain mobility of CS under stress thus improve the mechanical properties of CS/PGO nanocomposite membranes. PGO can also stop the propagation of micro-cracks due to the strong interfacial interaction between PGO layer and CS matrix, resulting in an increase of the elongation at break of CS/PGO nanocomposite membranes.

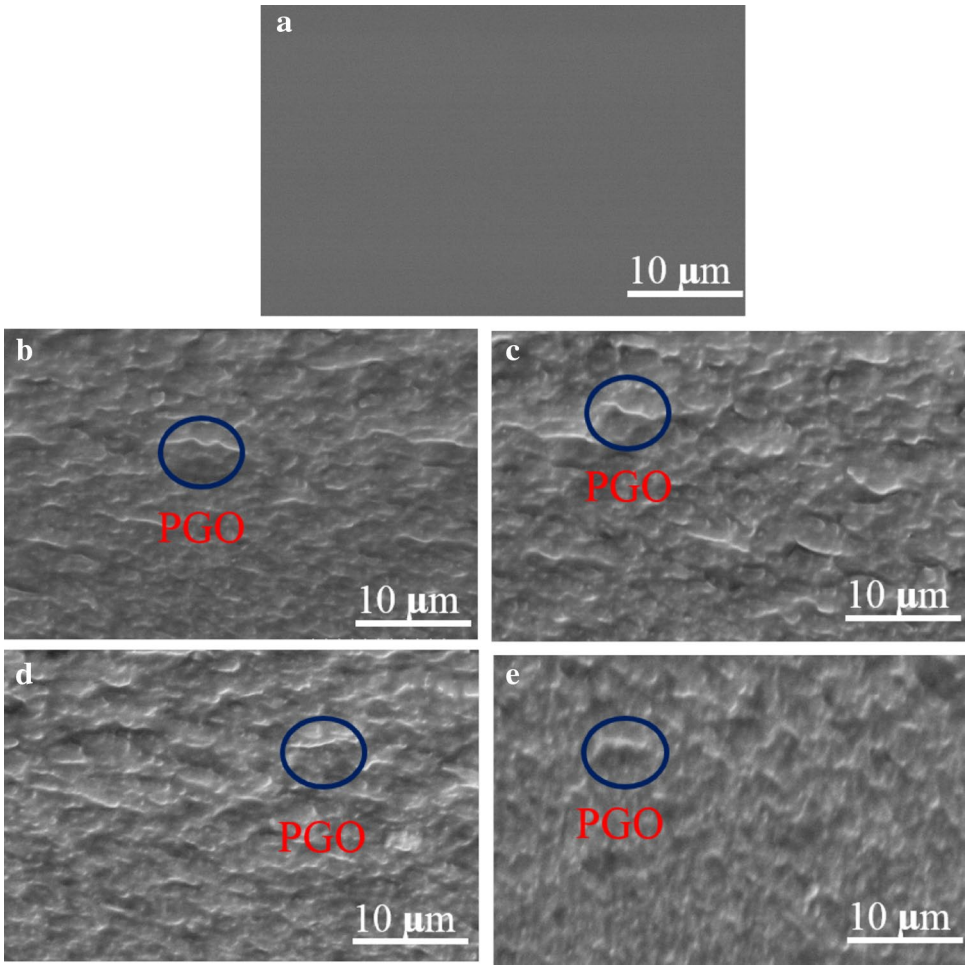

Fig. 10 SEM images of cryo-fractured surfaces of CS and CS/PGO nanocomposite membranes with different PGO contents. CS/PGO (0) (**a**), CS/PGO (1.0) (**b**), CS/PGO (1.5) (**c**), CS/PGO (2.0), and (**d**), CS/PGO (2.5) (**e**)

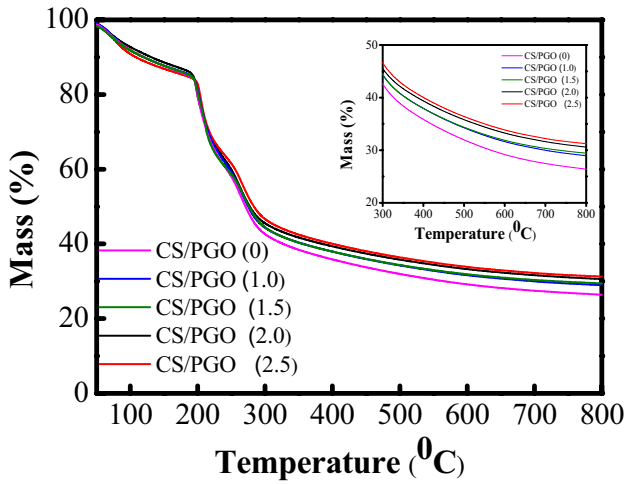

Fig. 11 TGA of CS/PGO nanocomposite membranes

3.2.3 Water uptake and area swelling of CS/PGO nanocomposite membranes

The composites for PEMFC applications should have a high water retention ability in order to achieve better performance and longer service life without significant deterioration caused by dehydration. A proton exchange membrane is typically comprised of both free and bound water. The membrane matrix with a high amount of bound water can offer adequate proton carriers and dissociate various proton conducting groups through solvation [44]. It is known that the water in a proton exchange membrane plays a vital role in proton conductivity because: (a) water molecules can improve the migration of protons by providing a proton medium (free water); (b) a hydrogen-bonded

Table 3 The mechanical properties of CS and CS/PGO nanocomposite membranes

Membranes	Tensile strength (MPa)	Elongation at break (%)
CS/PGO (0)	32.70 ± 3.27	8.19 ± 2.48
CS/PGO (1.0)	39.73 ± 0.88	5.08 ± 1.07
CS/PGO (1.5)	45.81 ± 0.08	10.63 ± 2.34
CS/PGO (2.0)	49.30 ± 1.43	10.88 ± 1.74
CS/PGO (2.5)	61.14 ± 1.22	11.82 ± 1.02

network (bound water) is formed; and (c) proton conducting groups are dissociated (free water). Nevertheless, excessive water uptake can lead to a reduction in the mechanical properties of the membrane because it can weaken the interaction between the CS chains. The water uptake of CS/PGO nanocomposite membranes is shown in Fig. 12a. Pure CS shows a water uptake of 65%, because hydrophilic –OH and $–NH_2$ groups can easily combine with water. However, CS/PGO nanocomposite membranes show a lower water uptake, and increasing the PGO content from 1 to 2.5 wt% results in a decrease in the water uptake from 61 to 50%. The strong interactions (electrostatic and hydrogen bond) between $–PO_3H_2$ groups of GO and $–NH_2$ group of CS can decrease the water storage sites of CS chains, resulting in a decrease in the water adsorption capacity of CS/PGO nanocomposite.

Water adsorption is the main reason for membrane swelling, and generally the higher the water uptake, the higher the swelling ratio of the proton exchange membrane. As shown in Fig. 12b, the area swelling decreases as the PGO content increases, and thus it follows the order of CS > C/PGO-1 wt% > CS/PGO-1.5 wt% > CS/PGO-2.0 wt% > CS/PGO-2.5 wt%. The pure CS shows an area swelling of 60%, whereas CS/PGO-2.5 wt% membrane shows an area swelling of 44%, indicating that CS/PGO nanocomposite membranes have better dimensional stability.

3.2.4 IEC and proton conductivity of CS/PGO nanocomposite membranes

Figure 13a shows that the IEC of the CS control membrane is 0.18 mmol g^{-1}. As expected, the IEC of CS/PGO nanocomposite membranes increases with the increase of PGO content, and a maximum of 0.53 mmol g^{-1} is achieved at 2.5 wt% PGO, which is about three times higher than that of CS because the phosphonic acid groups as proton carriers can significantly increase the IEC of the CS/PGO nanocomposite membranes.

Theoretically, there are two mechanisms for proton transfer in a membrane, including the Vehicle mechanism whereby protons are transported in the form of hydrated hydrogen ions, and the Grotthuss mechanism whereby protons are transported from one carrier to the next through hydrogen bonding network [65, 66]. The CS control membrane shows a proton conductivity of 0.011 S cm^{-1}, which is consistent with earlier reports [36]. The proton conductivity of Nafion 117 (0.033 S cm^{-1}) is used for comparison [67]. The increase of the PGO content from 1.0 to 2.0 wt%

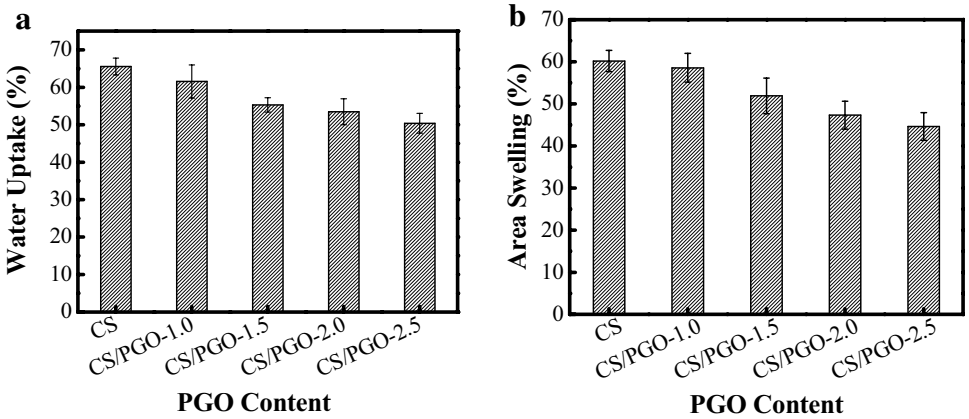

Fig. 12 **a** Water uptake and **b** area swelling of CS/PGO nanocomposite membranes

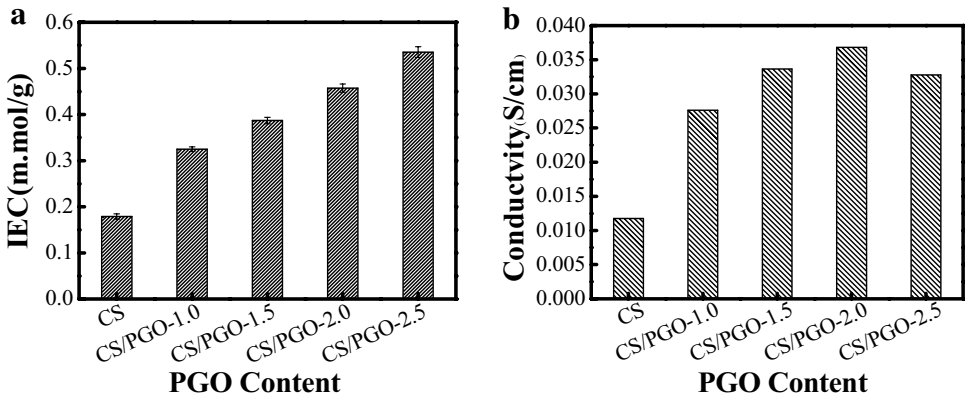

Fig. 13 **a** IEC and **b** proton conductivity of CS/PGO nanocomposite membranes

results in an increase in the proton conductivity from 0.027 to 0.036 S cm^{-1}, as shown in Fig. 13b. However, the proton conductivity is decreased to 0.032 S cm^{-1} with the further increase of the PGO content to 2.5 wt%, which can be attributed to the aggregation of PGO. Thus, the optimal PGO content is determined to be 2 wt%.

The proton conductivity of the CS/PGO nanocomposite membranes is enhanced due to the following reasons. The abundant phosphonic acid groups in the CS/PGO nanocomposite membranes can function as additional proton hopping sites. The phosphonic acid can accept and donate protons due to its amphoteric nature [68], and it can also act as a facile hopping site for proton transfer through the hydrogen bond network. The uniform dispersion of the two-dimensional PGO can provide long and wide proton transfer pathways. The proton transport in the CS/PGO nanocomposite membranes requires well connected channels formed by the phosphonate functional groups. The high density of the phosphonic acid sites due to the introduction of PGO can form transport channels with improved connectivity. Proton can be transported rapidly in these channels, resulting in an increase in the proton conductivity of the CS/PGO nanocomposite membranes with the increase of PGO content to 2 wt%. As the PGO content increases, the number of ion exchangeable site also increases, which can improve the proton mobility in the membrane. The particular sheet structure of PGO allows for the formation of continuous pathways by the hopping sites. The production of acid–base pairs ($–PO_3H^-\cdots{}^+H_3N–$) at the CS/PGO interface can accommodate the protonation/deprotonation of the acid/base groups, and thus the proton conductivity of the acid (PGO) and base (CS) groups can be improved simultaneously. Moreover, the proton conductivity of the nanocomposite membranes increases as the PGO content increases to 2 wt%, but it decreases at a PGO content of 2.5 wt% due to aggregation of PGO, which can decrease electrostatic and hydrogen bonding interactions. Similar phenomena are also observed by other researchers [36].

4 Conclusions

In the present work, GO was phosphorylated and then incorporated into CS for the preparation of CS/PGO nanocomposite membranes. The proton conductivity of these nanocomposite membranes is enhanced with the incorporation of PGO. The CS/PGO (2.0 wt%) nanocomposite membrane shows higher proton conductivity compared with commercially available Nafion 117 membrane. The incorporation of PGO can inhibit the mobility of CS chains, resulting in an increase in thermal and mechanical stability of CS/PGO nanocomposite membranes. These nanocomposite membranes also show a lower water uptake due to the decrease in $–NH_2$ functional group of the CS. This study provides a facile way to fabricate highly conductive nanocomposite membranes for energy related applications.

Acknowledgements This research is financially supported by the National Natural Science Foundation of China (Grant No. 51463020), Kunlun Scholar Award Program of Qinghai Province and Thousand Talents Program of Qinghai Province.

References

1. J. Dang, L. Zhao, J. Zhang, J. Liu, J. Wang, J. Membr. Sci. **545**, 88 (2018)
2. X. Zhang, T. Ai, Y. Huang, Y. Zhao, L. Han, J. Lu, J. Nanosci. Nanotech. **19**, 98 (2019)
3. Y. Ou, W.-C. Tsen, S.-C. Jang, Electrochim. Acta **264**, 251 (2018)
4. V. Vijayalekshmi, D. Khastgir, Cellu. **25**, 661 (2018)
5. Y. Cai, Z. Yue, Q. Jiang, S. Xu, J. Energ. Chem. **27**, 820 (2018)
6. M. Tariq, W.Q. Zaman, W. Sun, A.C.S. Sust, Chem. Eng. **6**, 4854 (2018)
7. Y.-L. Liao, C.-C. Hu, J.-Y. Lai, Y.-L. Liu, J. Membr. Sci. **531**, 10 (2017)
8. W. Wang, B. Shan, L. Zhu, C. Xie, C. Liu, F. Cui, Carbohydr. Polym. **187**, 35 (2018)
9. K. Wang, L. Yang, W. Wei, L. Zhang, G. Chang, J. Membr. Sci. **549**, 23 (2018)
10. S. Ahmed, Y. Cai, M. Ali, S. Khannal, S. Xu, Mater. Exp. **9**, 42 (2019)
11. L. Han, X. Luo, X. Luan, C. Wang, Y. Zhao, J. Lu, Int. J. Hydrog. Energy **41**, 15783 (2016)
12. K. Schmidt-Rohr, Q. Chen, Nat. Mater. **7**, 75 (2008)
13. A. Saad, C. Yangben, A. Muhammad, K. Santosh, X. Shiai, J. Appl. Polym. Sci. **136**, 46904 (2019)
14. A.U. Devi, K. Divya, N.J. Kaleekkal, D. Rana, A. Nagendran, Polym. **140**, 22 (2018)
15. J.L. Lu, Q.H. Fang, S.L. Li, S.P. Jiang, J. Membr. Sci. **427**, 101 (2013)
16. X. Li, H. Ma, Y. Shen, J. Power Sources **336**, 391 (2016)
17. J. Fang, X. Lin, D. Cai, N. He, J. Zhao, J. Membr. Sci. **502**, 29 (2016)
18. J. Zeng, B. He, K. Lamb, R. De Marco, P.K. Shen, S.P. Jiang, Chem. Commun. **49**, 4655 (2013)
19. L. Vilciauskas, S.J. Paddison, K.-D. Kreuer, J. Phys. Chem. A **113**, 9193 (2009)
20. S.J. Paddison, K.-D. Kreuer, J. Maier, Phys. Chem. Chem. Phys. **8**, 4530 (2006)
21. T. Itoh, K. Hirai, M. Tamura, T. Uno, M. Kubo, Y. Aihara, J. Power Sources **178**, 627 (2008)
22. S. Li, Z. Zhou, M. Liu, Electrochm. Acta. **51**, 1351 (2006)
23. H. Wu, W. Hou, J. Wang, L. Xiao, Z. Jiang, J. Power Sources **195**, 4104 (2010)
24. G. He, L. Nie, X. HaJ, Power Sources. **259**, 203 (2014)
25. U. Lafont, L. Simonin, M. Gaberscek, E.M. Kelder, J. Power Sources **174**, 1104 (2007)
26. Y. Zhao, H. Yang, H. Wu, Z. Jiang, J. Power Sources **270**, 292 (2014)
27. V.V. Binsu, R.K. Nagarale, V.K. Shahi, P.K. Ghosh, React. Funct. Polym. **66**, 1619 (2006)
28. W. Ying, K.A.M. Creber, P. Brant, B.V. Tam, Macromol. Chem. Phys. **204**, 850 (2003)
29. H. Steininger, M. Schuster, K.D. Kreuer, J. Maier, Solid State Ionics **177**, 2457 (2006)

30. G.-B. Jung, C.-C. Tseng, C.-C. Yeh, C.-Y. Lin, Int. J. Hydrog. Energy **37**, 13645 (2012)
31. F.J. Nores-Pondal, M.P. Buera, H.R. Corti, J. Power Sources **195**, 6389 (2010)
32. H. Pu, D. Wang, Electrochm. Acta. **51**, 5612 (2006)
33. Y. Li, G. He, S. Wang, J. Mater. Chem. A **1**, 10058 (2013)
34. H. Bai, Y. Li, H. Zhang, J. Membr. Sci. **495**, 48 (2015)
35. S. Ahmed, M. Ali, Y. Cai, J. Appl. Polym. Sci. (2019). https://doi.org/10.1002/app.47603
36. Y. Liu, J. Wang, H. Zhang, J. Power Sources **269**, 898 (2014)
37. Y. Xiao, Y. Xiang, R. Xiu, S. Lu, Carbohydr. Polym. **98**, 233 (2013)
38. Y. Wan, B. Peppley, K.A.M. Creber, V.T. Bui, E. Halliop, J. Power Sources **162**, 105 (2006)
39. N. Cao, C. Zhou, Y. Wang, H. Ju, D. Tan, J. Li, Materials **11**, 516 (2018)
40. Z. Tang, Z. Zhang, Z. Han, S. Shen, J. Li, J. Yang, J. Mater. Sci. **51**, 8791 (2016)
41. H. Beydaghi, M. Javanbakht, Ind. Eng. Chem. Res. **54**, 7028 (2015)
42. L. Wang, A. Lai, Y. Zhuo, Q. Zhang, A. Zhu, Q. Liu, CIESC J **66**, 3605 (2015)
43. J. Kalaiselvimary, M.R. Prabhu, J. Mater. Sci.: Mater. Electron. **29**, 5525 (2018)
44. R.P. Pandey, V.K. Shahi, RSC Adv. **4**, 57200 (2014)
45. Y. Wan, K.A. Creber, B. Peppley, V.T. Bui, Polym. **44**, 1057 (2003)
46. N. Shaari, S.K. Kamarudin, J. Power Sources **289**, 71 (2015)
47. H. Bai, H. Zhang, Y. He, J. Liu, B. Zhang, J. Wang, J. Membr. Sci. **454**, 220 (2014)
48. G. Zhao, T. Wen, X. Yang, Dalton Trans. **41**, 6182 (2012)
49. D. He, Z. Peng, W. Gong, Y. Luo, P. Zhao, L. Kong, RSC Adv. **5**, 11966 (2015)
50. G. He, J. Zhao, S. Hu, ACS Appl. Mater. Interfaces **6**, 15291 (2014)
51. L. Ma, X. Yang, L. Gao, Carbon **53**, 269 (2013)
52. C. Xu, X. Wu, J. Zhu, X. Wang, Carbon **46**, 386 (2008)
53. H.-J. Shin, K.K. Kim, A. Benayad, Adv. Funct. Mater. **19**, 1987 (2009)
54. K. Hatakeyama, M.R. Karim, C. Ogata, Chem. Comm **50**, 14527 (2014)
55. S. Wang, P.K. Ang, Z. Wang, A.L.L. Tang, J.T. Thong, K.P. Loh, Nano Lett. **10**, 92 (2009)
56. J. Liu, T. Zhang, Z. Wang, G. Dawson, W. Chen, J. Mater. Chem. **21**, 14398 (2011)
57. M. Scagliotti, M. Villa, G. Chiodelli, J. Non-Cryst. Solids **93**, 350 (1987)
58. L. Nie, J. Wang, T. Xu, H. Dong, H. Wu, Z. Jiang, J. Power Sources **213**, 1 (2012)
59. B. Smitha, S. Sridhar, A.A. Khan, J. Power Sources **159**, 846 (2006)
60. H. Liu, C. Gong, J. Wang, Carbohydr. Polym. **136**, 1379 (2016)
61. J. Ma, Y. Sahai, Carbohydr. Polym. **92**, 955 (2013)
62. J.F. Du, Y. Bai, W. Chu, J. Qiao, Polym. Sci. Part. B: Polym. Phys. **48**, 880 (2010)
63. A. Shirdast, A. Sharif, M. Abdollahi, J. Power Sources **306**, 541 (2016)
64. Y. Wang, D. Yang, X. Zheng, Z. Jiang, J. Li, J. Power Sources **183**, 454 (2008)
65. S. Peighambardoust, S. Rowshanzamir, M. Amjadi, Int. J. Hydrog. Energy **35**, 9349 (2010)
66. L. Vilčiauskas, M.E. Tuckerman, G. Bester, S.J. Paddison, K.-D. Kreuer, Nat. Chem. **4**, 461 (2012)
67. H. Liu, J. Wang, S. Wen, J. Appl. Polym. Sci. **133**, 45 (2016). https://doi.org/10.1002/app.43070
68. S.-I. Lee, K.-H. Yoon, M. Song, Chem. Mater. **24**, 115 (2011)